COMMUNICATION

Check for updates

Functionalisation of graphite and thermally reduced graphene oxide with bis-hydrazone copper(I) nitrate salt†

Piotr W. Zabierowski, [ID] *[a] Lukáš Děkanovský,[a] Vlastimil Mazánek,[a] Maciej Hodorowicz[b] and Zdeněk Sofer [ID] *[a]

The solvothermal functionalization of graphite and thermally reduced graphene oxide (TRGO) using a bis-hydrazone copper(I) complex is demonstrated. This treatment resulted in a remarkable 328% increase in the BET specific surface area of graphite, reaching 374 m^2 g^{-1}, while the surface area of TRGO remained unchanged. The hybrid composites show promise as potential components for gas sensors.

The remarkable properties exhibited by two dimensional (2D) materials have revolutionized the landscape of modern materials science and engineering. Graphene, the prototypical 2D material,[1] garnered immense attention for its exceptional mechanical,[2] electronic[3] and thermal[4] characteristics. Since then, a diverse family of 2D materials, including transition metal dichalcogenides (TMD),[5] black phosphorus,[6] and MXenes,[7] has emerged, each possessing unique properties that make them highly attractive for a wide array of applications.

However, to fully harness the potential of 2D materials and integrate them seamlessly into various technological platforms, it is imperative to go beyond their intrinsic properties. This is where functionalization plays a pivotal role.[8–10] Functionalization involves the deliberate modification of the

[a]University of Chemistry and Technology Prague, Technická 5, Prague, 166 28 Czech Republic. E-mail: zabierop@vscht.cz, soferz@vscht.cz
[b]Faculty of Chemistry, Jagiellonian University, Gronostajowa 2, 30-387 Kraków, Poland

†Electronic supplementary information (ESI) available: Crystal data and structure refinement details, bond lengths and angles, hydrogen bond geometry, UV-VIS absorption spectra for complex 1, simulated IR spectra for complex 1 and 2, simulated Raman spectra for 1 and 2, simulated UV-VIS-NIR absorption spectra for 1 and 2, ascription of the strongest vibrations in simulated IR spectra, FESEM images with elemental mapping for graphite, TRGO and TRGO-Cu2 hybrid composite, EDX spectra, XPS spectra with deconvolution of selected bands, FTIR spectral data for complexes 1 and 2, COSY NMR for complex 1, HRMS spectrum for complex 1, details of preparation of the complexes and hybrid composites, description of characterisation of the materials. CCDC 1590016 (for **1**) and 2348643 (for **2**) include the supplementary crystallographic data for this work. For ESI and crystallographic data in CIF or other electronic format see DOI: https://doi.org/10.1039/d4nr03456b

surface or edges of 2D materials with specific chemical groups, nanoparticles, or molecules. This process imparts additional functionalities to the 2D material, allowing for tailored properties that are finely tuned to meet the demands of targeted applications.

Bishydrazone complexes emerge as compelling candidates for the molecular grafting of graphene layers owing to their versatile chemical properties. Thanks to π-conjugated nature they form self-assembled monolayers on Highly Oriented Pyrolytic Graphite.[11,12] These types of complexes feature hydrazone groups (=N–NH–) that exhibit remarkable properties in directing the complex assemblies[13] but also possess exceptional reactivity upon deprotonation. The deprotonated bishydrazone ligands were found to bind to fullerenes, forming pyrazoline rings.[14,15] Thus, our hypothesis is, that the bishydrazone copper(I) complex could bind to defect sites of graphite, as starting points for further growth of functional nanostructures. These nanocomposites could function as sensors owing to the fact that bishydrazones possess the quality of vapor sensing.[16] Up to our best knowledge, such systems, either sole ligands or complexes, have never been tested as impedimetric sensors for volatile vapours on interdigitated electrodes.
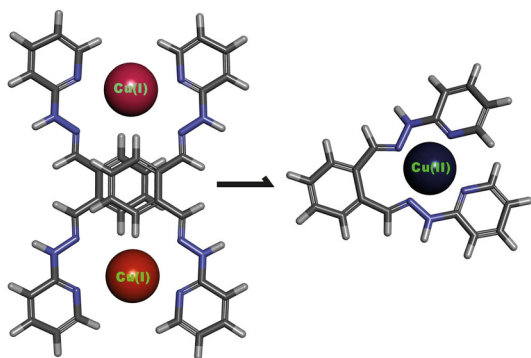
In this study, the usability and efficacy of bishydrazone copper(I) complex (Fig. 1) in the functionalization of 2D materials, specifically graphite and thermally reduced graphene oxide (TRGO), are demonstrated. The bishydrazone copper(I) complex exhibited a remarkable ability to interact selectively with defect sites inherent in the structure of graphite and TRGO. Through comprehensive spectroscopic analyses and surface characterization techniques, such as X-ray photoelectron spectroscopy (XPS), Scanning Electron Microscopy with EDX mapping, Transmission Electron Microscopy and Raman spectroscopy, the successful functionalization of these 2D materials was confirmed. The complex, owing to its tailored chemical structure and specific reactivity, showcased an impressive capability to anchor onto the surface of graphite and TRGO, thereby introducing desirable functionalities and enhancing the

Fig. 1 The coordination modes of bis-hydrazone ligand (1,2-di[[2-(pyridin-2-yl)hydrazin-1-ylidene]methyl]benzene): bridging bis-bidentate (left) and chelating tetradentate (right) towards copper(I) and copper(II) in this work. Dinuclear complex can be converted to mononuclear copper(II) in presence of ammonium fluoride and pyridine in open system conditions.

materials' properties (specific surface area, pore volume and impedimetric sensing property).

Complex **1** crystallizes in monoclinic crystal system and space group $P2_1/n$ (detailed data collection details, crystal data and structural data are included in ESI in Tables S1–S8†). The molecular structure is dinuclear, and one ligand and one tetrahedrally coordinated copper(I) centre (CuN₄) are in the asymmetric unit (Fig. 2A). The mode coordination of the bis-hydrazone ligand is bis-bidentate bridging, with metal–metal separation reaching 7.60 Å. The plane of the phenyl ring of the central part of the ligand is oriented with respect to the plane of the pyridyl ring under an angle of 36.4 degrees, and is coplanar with the mean plane of the hydrazone group. The double bond configuration is *Z,Z* and the overall symmetry of the molecule of the complex dication **1** is C_i with inversion centre at the center of gravity of the molecule. In contrast, complex **2** (molecular structure presented in Fig. 2B) crystallizes in orthorhombic crystal system and *Pbca* space group. Copper(II) adapts distorted trigonal bipyramid coordination geometry composed of CuN₄O atoms (O atom from nitrate). The –NH–N= groups are directed towards each other, in a tetradentate chelating mode (with a rare seven-membered chelate ring in

boat conformation). The mean atomic planes of pyridine rings are directed differently with respect to the mean *o*-phenyl plane than in complex **1**, under angles 21.5 and 56.6 degrees. Interestingly, despite different mode of coordination of the ligand, the shortest copper–copper distance in the structure of complex **2** is smaller than in case of **1**, being equal to 7.07 Å.

In the arrangement of molecular ions in the salt **1**, the prevailing forces are charge assisted hydrogen bonds (nitrate *vs.* complex dication), conventional hydrogen bonds (ethanol solvate donates to nitrate), π–π stacking (complex dication *vs.* complex dication) and anion–π (nitrate *vs.* complex dication) interactions. While the mentioned hydrogen bonds form discrete assemblies, the π–π stacking interactions are dominating in the long range, contributing to assemblage of herringbone motif, presented in Fig. 3A, in the structure of the complex salt. On the other hand, the crystal packing in complex **2** is more complicated, despite the fact that the compound is not a solvate (Fig. 3B). The [CuL(NO₃)]⁺ cations are gathered together in dimers, through anion–π intermolecular interaction (pyridyl-nitrate). Further, the anions are assembled thank to charge assisted hydrogen bonds (hydrazone groups *vs.* nitrates) and anion–π interactions in which both the phenyl and pyridyl rings are involved. The overall supramolecular structure in complex **2** is three dimensional. The structures of complex **1** and **2** represent a example of lack of oxidation isomerism (redox reversibility), where with one ligand both dinuclear and mononuclear compounds can be distinguished with metal cation at different oxidation states. An example of coordination isomerism can be found in case of helicate and pincer lanthanide complexes,[17] although they comprise no oxidation state isomerism as in case of tin complexes[18] with *o*-iminoquinone ligands.

The FT-ATR-IR spectra for complex **1** and complex **2** (Fig. S3†) contain characteristic absorptions for functional groups present in their structures. The IR and Raman spectra were simulated for the complex ions [Cu₂L₂]²⁺ and [CuL(NO₃)]⁺ at B3LYP LANL2DZ level of theory in the gas phase (Tables S9–S11 and Fig. S4–S5 in the ESI†), to aid interpretation of the experimental spectra. There is a significant shift of the bands corresponding to imine stretching vibrations registered for solids and calculated for the gas phase ions. Whereas the most
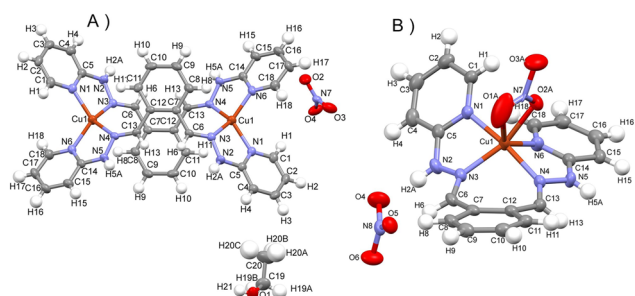

Fig. 2 The molecular structures of complex **1** (A) and **2** (B) with atom labelling. Thermal ellipsoids represent 50% probability, nitrate ions disordered over two sets of sites are shown for one set in part B.

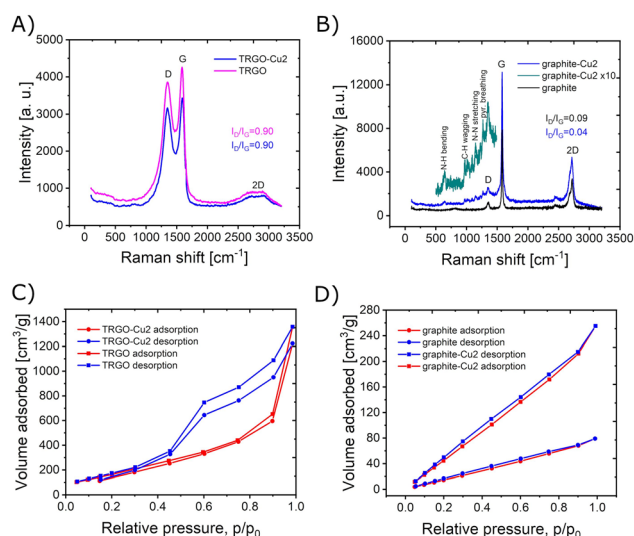**Fig. 3** The motifs in crystal packing of complex **1** (A) and **2** (B). Thermal ellipsoids represent 50% probability.

intense imine stretching absorptions occur at 1616 and 1625 cm^{-1} ($\nu_{C=N}$, for **1** and **2**, respectively), for the gas phase (calculated) they are slightly shifted towards lower energy: 1603 and 1623 cm^{-1} for [Cu$_2$L$_2$]$^{2+}$ and 1565, 1654, 1648 and 1644 cm^{-1} for [CuL(NO$_3$)]$^+$. In the case of the last three frequencies they are combination bands together with pyridine ring breathing modes. Similar breathing modes of vibrations are responsible for strong absorptions around 1480 cm^{-1} from both complexes **1** and **2** in the solid state, concomitant with the data reported for 1-iminoisoindoline complexes.[19] Another set of strong absorptions occur around 1300 cm^{-1} (1284 cm^{-1} for **1** and 1303 cm^{-1} for **2**), which can be ascribed to ν_{C-N} in hydrazone groups and pyridine rings (1302 cm^{-1} for **2** in the gas phase calculation). The strong bands located around the mentioned ν_{C-N}, should belong to the nitrate ν_{N-O}, which for the gas phase occur at 1130 cm^{-1} and 926 cm^{-1} for complex **2**. The nitrate $\nu_{N=O}$ occurs for the gas phase at 1439 cm^{-1} and is included in combination mode with ω_{C-H} of pyridine rings and ω_{C-H} of the imine group. At lower energies, the out-of-plane C–H bending vibration of pyridine rings occurs for the gas phase at 806 cm^{-1}, which are also present in solid state spectra at 763 and 769 cm^{-1} for **1** and **2**, respectively. The solid state spectrum of **1** contains also strong absorption bands positioned at 483 cm^{-1}, which can be ascribed to bending of –N–H in hydrazone groups (498 cm^{-1}) or scissoring mode of the hydrazone N–H and imine C–H bonds (482 cm^{-1}). Finally, in the high energy region of the spectrum occur bands associated with imine ν_{C-H} and hydrazone ν_{N-H} vibrations which for the gas phase calculations occur at 3109 cm^{-1} and 3578 cm^{-1} for complex **1** and at 3105 and 3586 cm^{-1} for complex **2**. Compared to solid state spectra of **1** and **2**, there is a large discrepancy stemming from the fact that gas phase molecules do not take part in hydrogen bonding. Here, the intermolecular interactions contribute to lowering of the vibrational energies, and due to Z larger than **1**, the multiplicity of vibrational frequencies is enlarged. Generally, the ν_{N-H} occur at around 3345–3360 cm^{-1} and the ν_{C-H} in between 2794–3100 cm^{-1} range of wavenumbers.

The crystalline phase of complex **2** contained phase of complex **1** and thus we have chosen only complex **1** for functionalisation study.

The functionalisation of graphite and reduced graphene oxide was conducted under solvothermal conditions in the presence of a mild base, triethylamine. The complex **1** is well soluble in methanol and other solvents, such as acetonitrile, ethanol, chloroform and polar solvents such as dimethylformamide and dimethylsulfoxide (ESI, the UV-VIS absorption spectra – Fig. S6, HRMS spectrum in methanol – Fig. S7, ^{1}H NMR spectrum in DMSO – Fig. S8, COSY spectrum in DMSO – Fig. S9†). Methanol was chosen as the main solvent for further treatments. Additionally, inert conditions of Argon atmosphere were maintained during the reaction of functionalisation. After isolation of the materials by centrifugation, they were washed with methanol and dried at elevated temperature in air. The solids were a subject of characterisation with PXRD, Raman spectroscopy, FE-SEM, TEM, EDX, XPS and BET analysis.

The PXRD pattern of the graphite-Cu2 composite (Fig. S10 in ESI†) confirms the integrity of graphite structure after the functionalisation. Only a small shift of the main diffraction peak towards lower 2θ angle was recorded (from 27.21 to 26.97 2θ degrees). The FWHM value also changed for the 002 hkl peak, from 0.29 2θ to 0.18 2θ. From the Scherrer equation[20] the average grain size was calculated.[21] This increased from 28 nm to 45 nm, thus it is a considerable change of grain size after functionalisation. The reason of such behavior can be a consequence of consumption of smaller crystallites and their solubilisation in the process of functionalisation. In contrast, the PXRD pattern recorded for TRGO is very similar to original, after functionalisation (Fig. S11†). The functionalisation did not improve the crystallinity of the TRGO.

The Raman spectra of TRGO and TRGO-Cu2 composite are shown in Fig. 4A. The structural integrity of TRGO was not affected since the spectrum after functionalisation was negligibly modified. In terms of I_D/I_G = 0.90 ratio it remained unchanged. However, the D band shifted from 1357 to 1342 cm^{-1} and G band shifted from 1585 to 1592 cm^{-1}. Interaction between the graphenic regions of TRGO and the bis-hydrazone complex, likely through π–π stacking interactions, is probably responsible for the observed change in Raman shifts of these bands. The Raman spectra for the graphite and graphite-Cu2 composite are shown in Fig. 4B. The graphite spectrum shows the typical D and G bands positioned at 1357 and 1579 cm^{-1} (I_D/I_G = 0.09) while the 2D and 2G bands are located at 2442 and 2720 cm^{-1}. After functionalisation with [Cu$_2$L$_2$]$^{2+}$ new peaks arrive in the Raman spectrum, at 640, 976, 1093, 1147, 1226 and 1266 cm^{-1}. These low intensity bands can be ascribed to presence of the complex **1** (ESI Fig. S5†). The D peak is shifted to 1348 cm^{-1}, while the G peak

Fig. 4 The characterisation data for complexes and composites: (A) and (B) Raman spectra for TRGO and TRGO-Cu2 composite and graphite, graphite-Cu2 composite with enlarged part of spectrum below 1500 cm^{-1}; (C) and (D) N$_2$ sorption isotherms at 77 K for the starting materials and composites with complex **1**.

remains at the same position at 1580 cm^{-1}. The I_D/I_G = 0.04 decreased, indicating the most probably a slight decrease in number of defect sites, thus a slight increase of graphite crystallinity and quality.

The FE-SEM images of the starting materials and hybrid composites are presented in Fig. 5 and Fig. S12–S17 (ESI†). They show that graphite contains layered grain morphology with presence of delaminated layers and small stacks. On the other hand, the TRGO shows a highly porous structure with terraces and folded surfaces. At the macroscale, there is no significant change in morphology after functionalisation of both materials. However, the EDX elemental mapping, shown in Fig. 5, S12 and S13 (ESI†), clearly indicates almost uniform coverage with copper for both materials. The yellow circle in Fig. 5 depicts the edges of graphite grain, which contain more copper than surroundings. This fact, could explain the role of the complex 1 in functionalisation and generation of slit type of porosity.

The XPS spectra (Fig. S18–S21 in ESI†) and EDX spectra (Fig. S22 and S23 in ESI†) confirm the composition of the starting materials and hybrids. At the survey spectra for graphite-Cu2 and TRGO-Cu2 composite the presence of copper is confirmed, and the most probably it is copper(ı), since the satellite bands are not detected.[22] Therefore in the process of functionalisation the oxidation state of copper is maintained. Additionally, the presence of three types of nitrogen functionalities (398.4, 399.4 and 400.7 eV) is concluded from the deconvolution spectra which correspond to pyridine[23] and hydrazone (–NH– and –N=) nitrogen functional groups.[24] The nitrate nitrogen is not seen (expected signal at 407.4 eV),[25] which confirms the deprotonated state of the $[Cu_2L_2]^{2+}$ cation, to become neutral charge after loosing two protons. Therefore, the most probable mode of interaction with graphite and TRGO might be a mixture of non-covalent and covalent, that is hydrogen bonding of protonated hydrazone, possibly reaction

with defect sites, C=O or –COO functional groups, and also π–π stacking interactions with graphenic regions. This assumption could be partially confirmed based on Raman spectrum of the graphite-Cu2 hybrid, which contains spectral features of the complex 1 whereas the Raman spectrum of TRGO-Cu2 does not.

The isotherms of nitrogen adsorption at 77 K are presented in Fig. 4C and D, for the materials before and after the functionalisation with complex 1. As can be seen, the functionalisation of graphite resulted in increase of specific surface and pore volume (Table 1). The shape of the isotherm for graphite-Cu2 corresponds to type II isotherm according to the Brunauer classification. It is characteristic to powders with large pores. The shallow hysteresis loop can be ascribed as type B of de Boer classification, which is associated with slit-shaped pores.[26] The specific surface area increased from 114 m^2 g^{-1} (graphite) to 374 m^2 g^{-1} (graphite-Cu2). In contrast, the functionalisation of reduced graphene oxide does not produce a significant change in specific surface area, remaining at slightly lower value of 677 m^2 g^{-1} (for TRGO-Cu2 sample). The hysteresis of desorption observed for samples of TRGO indicates the role of micropores and can be ascribed to type IV adsorption/desorption isotherm.

To gain insight into the morphology of the graphite-Cu2 composite, it was characterized with HRTEM. Fig. 6 presents the images of the graphite-Cu2 flake.

On the surface of the flake, the slit-type mesopores can be seen. Additionally, the edges of the flake are covered with a material of amorphous morphology. The graphite crystallographic planes can also be seen at the edges, with an interlayer distance of 3.4 Å.

To verify the applicability of the synthesized hybrid composites in the design of sensors, the experiments with gold-interdigitated electrodes (GIEs) were conducted in the presence of vapours of selected solvents (ethanol – EtOH, tetrahydrofuran – THF, acetonitrile – MeCN and toluene). The surface of GIE was modified with the hybrid composites by drop-casting a few microliters of the stock suspension (0.25 mg mL^{-1}) in dichloromethane. Then, the electrode was inserted in the saturated vapours of the above-mentioned solvents and the EIS spectra were collected (Fig. 7).

For ethanol, the electrochemical semicircle resistances behave like R(TRGO-Cu2) = 0.10 MΩ > R(GIE) = 0.078 MΩ > R(graphite-Cu2) = 0.030 MΩ showing a substantial drop in resistance for the graphite-Cu2 hybrid. For tetrahydrofuran the semicircle resistances behave like: R(GIE) = 4.8 MΩ > R(graphite-Cu2) = 0.92 MΩ > R(TRGO-Cu2) = 0.57 MΩ, while for acetonitrile they behave like R(graphite-Cu2) = 2.7 MΩ >
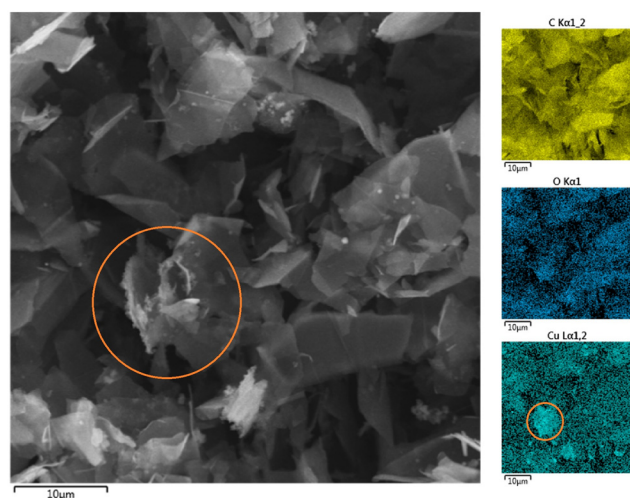

Fig. 5 The FE-SEM images of graphite-Cu2 composite together with EDX elemental mapping.

Table 1 Surface area (SSA) and pore volume (V_p) data

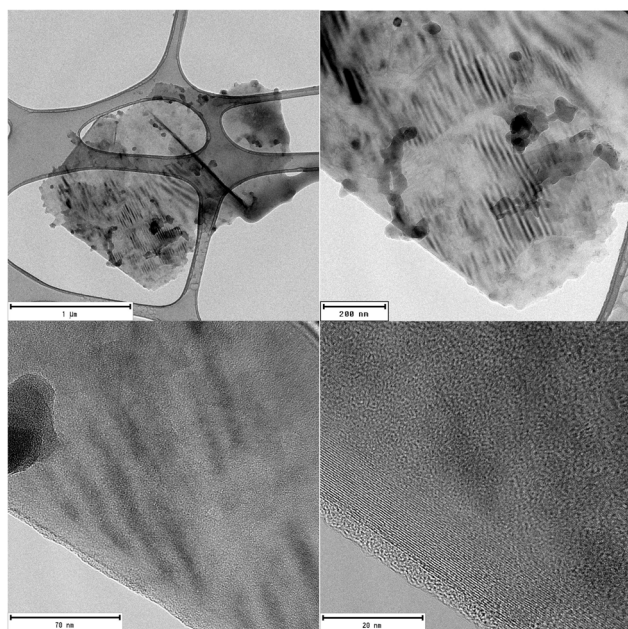| Sample	SSA [m^2 g^{-1}]	V_p [cm^3 g^{-1}]
TRGO	677	1.55
TRGO-Cu2	687	1.36
Graphite	114	0.10
Graphite-Cu2	374	0.31

Fig. 6 The HRTEM images of graphite-Cu2 composite flake.

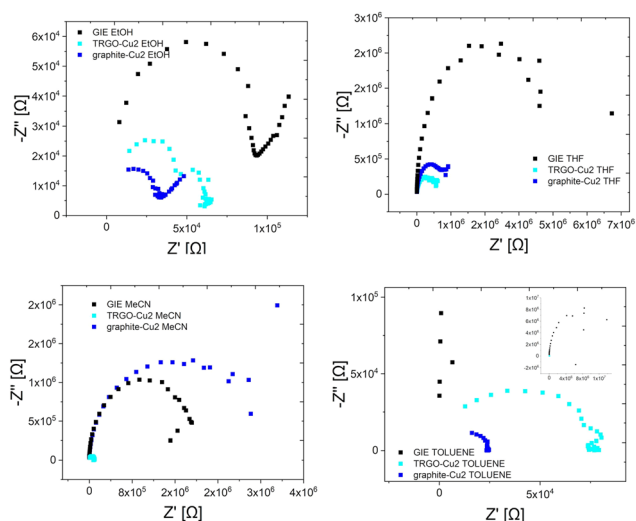**Fig. 7** The impedance spectra for different solvents for the GIE modified with the hybrid composites.

R(GIE) = 2.0 MΩ > R(TRGO-Cu2) = 0.052 MΩ. For toluene, the semicircle resistance behaves like: R(GIE) = 11.44 MΩ > R(TRGO-Cu2) = 0.080 MΩ > R(graphite-Cu2) = 0.013 MΩ. Interestingly, the TRGO-Cu2 sensor shows selectivity towards acetonitrile, with a significant drop in semicircle resistance. These promising results prove that the potential application of the hybrid composites in the sensor design is relevant, due to high specific surface areas and highly conjugated (conductive) bis-hydrazone copper(ı) complex molecules with exposed binding pockets.

In this work, we demonstrated for the first time the functionalisation of graphite and reduced graphene oxide with a bishydrazone complex of copper(ı). Additionally, we identified and characterized complexes with the same ligand and different oxidation states of copper. Moreover, we have demonstrated the potential of the synthesised composites in the design of gas sensors.

Data availability

The data supporting the findings of this study are available in the Zenodo repository at **https://doi.org/10.5281/zenodo.13772530**.

Conflicts of interest

There are no conflicts to declare.

Acknowledgements

References

1 L. E. F. Torres, S. Roche and J.-C. Charlier, *Introduction to graphene-based nanomaterials: from electronic structure to quantum transport*, Cambridge University Press, 2014.

2 D. G. Papageorgiou, I. A. Kinloch and R. J. Young, *Prog. Mater. Sci.*, 2017, **90**, 75–127.

3 K. S. Novoselov, S. V. Morozov, T. M. G. Mohinddin, L. A. Ponomarenko, D. C. Elias, R. Yang, I. I. Barbolina, P. Blake, T. J. Booth, D. Jiang, J. Giesbers, E. W. Hill and A. K. Geim, *Phys. Status Solidi B*, 2007, **244**, 4106–4111.

4 E. Pop, V. Varshney and A. K. Roy, *MRS Bull.*, 2012, **37**, 1273–1281.

5 A. V. Kolobov and J. Tominaga, *Two-dimensional transition-metal dichalcogenides*, Springer, 2016, vol. 239.

6 Z. Azizi, M. Ghashghaee and M. Ghambarian, *Black Phosphorus: Synthesis, Properties and Applications*, 2020.

7 B. Ansori and Y. Gogotsi, *2D metal carbides and nitrides (MXenes): structure, properties and applications*, Springer Nature Switzerland AG, 2019.

8 V. Georgakilas, *Functionalization of graphene*, John Wiley & Sons, 2014.

9 K. Zhang, *Chemically derived graphene: Functionalization, properties and applications*, Royal Society of Chemistry, 2018, vol. 46.

10 E. Celasco and A. N. Chaika, *Handbook of Graphene, volume 1: Growth, synthesis, and functionalization*, John Wiley & Sons, 2019.

11 G. Pace, A. Stefankiewicz, J. Harrowfield, J.-M. Lehn and P. Samorì, *ChemPhysChem*, 2009, **10**, 699–705.

12 A. R. Stefankiewicz, G. Rogez, J. Harrowfield, M. Drillon and J.-M. Lehn, *Dalton Trans.*, 2009, 5787–5802.

13 P. Zabierowski, M. Hodorowicz and J. Szklarzewicz, *New J. Chem.*, 2018, **42**, 817–821.

14 R. Caballero, M. Barrejon, J. Cerda, J. Arago, S. Seetharaman, P. de la Cruz, E. Orti, F. Dśouza and F. Langa, *J. Am. Chem. Soc.*, 2021, **143**, 11199–11208.

15 V. Cuesta, M. Urbani, P. de la Cruz, L. Welte, J.-F. Nierengarten and F. Langa, *Chem. Commun.*, 2016, **52**, 13205–13208.

16 M. Chang, A. Kobayashi, K. Nakajima, H.-C. Chang and M. Kato, *Inorg. Chem.*, 2011, **50**, 8308–8317.

17 R. Chen, Q.-Q. Yan, S.-J. Hu, X.-Q. Guo, L.-X. Cai, D.-N. Yan, L.-P. Zhou and Q.-F. Sun, *Org. Chem. Front.*, 2021, **8**, 2576–2582.

18 M. G. Chegerev, A. V. Piskunov, A. A. Starikova, S. P. Kubrin, G. K. Fukin, V. K. Cherkasov and G. A. Abakumov, *Eur. J. Inorg. Chem.*, 2018, **2018**, 1087–1092.

19 P. Zabierowski, D. Matoga and W. Nitek, *RSC Adv.*, 2015, **5**, 25911–25918.

20 D. J. Lim, N. A. Marks and M. R. Rowles, *Carbon*, 2020, **162**, 475–480.

21 A. Milev, M. Wilson, G. K. Kannangara and N. Tran, *Mater. Chem. Phys.*, 2008, **111**, 346–350.

22 T. Ivanova, K. Maslakov, A. Sidorov, M. Kiskin, R. Linko, S. Savilov, V. Lunin and I. Eremenko, *J. Electron Spectrosc. Relat. Phenom.*, 2020, **238**, 146878.

23 M. Camalli, F. Caruso, G. Mattogno and E. Rivarola, *Inorg. Chim. Acta*, 1990, **170**, 225–231.

24 M. Döring, M. Rudolph, E. Uhlig, V. Nefedov and J. Salyn, *Z. Anorg. Allg. Chem.*, 1987, **554**, 217–226.

25 S. Aduru, S. Contarini and J. W. Rabalais, *J. Phys. Chem.*, 1986, **90**, 1683–1688.

26 J. Han, K. Cho, K.-H. Lee and H. Kim, *Carbon*, 1998, **36**, 1801–1810.